FEASIBILITY STUDY OF X-RAY DIFFRACTION FOR A PORTABLE INSPECTION SYSTEM

Angela PETERZOL[1], Philippe DUVAUCHELLE[1], Valérie KAFTANDJIAN[1], and Pascal PONARD[2]

[1]CNDRI (Nondestructive Testing using Ionizing Radiation) Laboratory, INSA-Lyon, 69621 Villeurbanne, France

[2]THALES COMPONENTS & SUBSYSTEMS, 2 rue Marcel Dassault 78941 Vélizy cedex

1. Introduction

The X-ray transmission imaging has been widely used for security screening. The most efficient equipments include the dual-energy tomography, which allows materials discrimination in terms of their effective atomic number and density. However, this approach is inherently chemically non-specific because it is the molecular arrangement of the atoms in the material and not the atomic constituents alone that govern the chemical properties of a medium. In the past years, interest has been focused on the development of X-ray diffraction for the specific detection of materials. In particular, the energy-dispersive X-ray diffraction (EDXRD) has been pointed out to be well suited for the detection of narcotics and a wide range of explosives [1-10].

The work we present has been performed in the frame of a multi-partners research project, whose aim is the validation of a novel portable imaging system for the characterization of dangerous/illicit materials inside objects. The system combines two X-ray techniques: the dual-energy tomosynthesis and the energy-dispersive diffraction. The basic idea is to use the first technique to detect the suspicious regions inside an object. The role of the EDXRD is then to identify the suspected area by comparing the acquired spectrum with a database.

The 3D object exploration has to be performed without imposing any movements to the latter. Thus, in the diffraction modality, measurements are carried out by translating source and the sub-system output collimator/detector. The detector is based on CdZnTe (CZT) semiconductors, which can provide relative energy resolution ($\Delta E/E$) of about 3% @ 90 keV [11] at room temperature. Though the energy resolution is worse than that of detectors based on Ge semiconductors, the latter solution has been excluded for a portable system since Ge semiconductors need to be cooled in order to work properly. However, it has to be emphasized that the resolution furnished by CZT detectors has been proved to be sufficiently good for different material discrimination in the EDXRD [2,7,12,16-19,21].

In this paper, we report on work carried out to evaluate the experimental conditions (the high voltage of X-ray source, the diffraction angle θ, the angular resolution $\Delta\theta$, the collimators design, …) best suited for the system purposes. In order to clearly evaluate the influence of each parameter on the expected signal, the model based on the kinematic theory of diffraction has been exploited. The paper is organized as follows. The physical background for X-ray diffraction is recalled in section 2. In section 3, we discuss the choice of the diffraction angle θ and the high voltage of X-ray tube. Section 4 is devoted to the system resolution. In section 5 we give a brief description of the system set-up, while in section 6 we discuss the relation between the angular resolution and the collimators requirements.

2. Physical Background

Diffraction effects are observed when electromagnetic radiation impinges on periodic structures with geometrical variations on the length scale of the wavelength of the radiation. Following the

kinematic theory of diffraction (a detailed explanation can be found in [12-14]), we assume the case of a monochromatic plane wave, with K_0 the wave vector, impinging on a mono-crystallite as depicted on Fig. 2.1. The diffracted intensity I in the K direction and at a distance R from the crystal can be written, in the Fraunhofer case and for a non-polarized beam, as :

$$I(\vec{q}) = I_0 \frac{1}{R^2} \frac{d}{d\Omega} \sigma_T(\theta) |F(\vec{q})|^2 \zeta(\vec{q}) \qquad (2.1)$$

where q, the scattering vector, is equal to the wave vector difference $K - K_0$, θ is the angle between K and the prolonged direction of K_0, I_0 is the intensity of the incoming beam, $d\sigma_T(\theta)/d\Omega$ is the differential cross section for Thomson scattering, $F(q)$ is the crystal structure factor, and $\zeta(q)$ is the interference function.
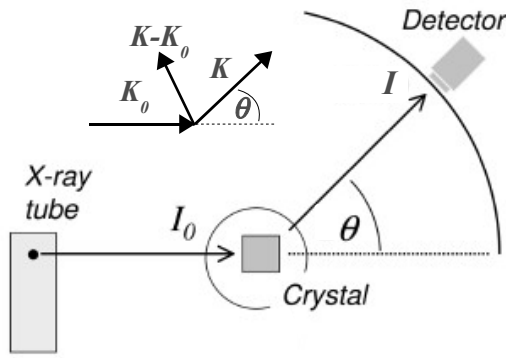
The structure factor F accounts of the incoming wave elastic scattering by the total charge distribution of the unit cell. It depends on the position of the atoms in the unit cell and their atomic scattering factor. The interference function ζ describes the distribution of the scattered intensity in the space around the crystallite. It contains the interference effects of the wave scattered by all the unit cells composing the crystal. Assuming the geometry of the simple cubic lattice, the interference function is given by

Fig. 2.1. Geometry configuration for X-ray diffraction.

$$\zeta(\vec{q}) = \prod_{i=1}^{3} \frac{\sin^2(N_i a \vec{q} \vec{c}_i/2)}{\sin^2(a \vec{q} \vec{c}_i/2)} \qquad (2.2)$$

where c_1, c_2 and c_3 are the unit vectors in the three orthogonal directions in the space, a is the cell parameter, and the three integers N_i give the length of the crystallite in units of cell edges. For large values of N_1, N_2 and N_3 the three factors in $\zeta(q)$ only differ from zero if the argument in the $\sin^2$ function of the denominator become integral multiple of π. Let us name these integers h, k and l in the following. The necessary condition to realize the highest intensity at R accordingly is

$$\begin{cases} a\vec{q}\vec{c}_1 = 2\pi h \\ a\vec{q}\vec{c}_2 = 2\pi k \\ a q c_3 = 2\pi l \end{cases} \qquad (2.3)$$

The set of equations (2.3) are the Laue conditions for the special case of cubic crystals. The magnitude of q when $I = I^{\max}$ can be obtained from the three conditional equations (2.3) by multiplying by the inverse cell parameter $1/a$, adding the squares and taking the square root. This yields as condition for maximum intensity

$$\left|\vec{(q)}\right| = 2\pi \frac{\sqrt{(h^2 + k^2 + l^2)}}{a} \qquad (2.4)$$

Now, using the facts that the magnitude of the scattering vector $|q| = 4\pi/\lambda \sin(\theta/2)$, with λ the photon wavelength, and the interplanar spacing d_{hkl} for cubic lattices is $a/\text{sqrt}(h^2 + k^2 + l^2)$, equation (2.4) tells us that to observe maximum intensity in the diffraction pattern of a simple cubic crystal

the following equation

$$\lambda = 2d_{hkl}\sin(\theta/2) \tag{2.5}$$

has to be obeyed. The equation (2.5) is called Bragg equation and was applied by W.H. Bragg and W.L. Bragg in 1913 to describe the position of X-ray scattering peaks in angular space. The Laue conditions and the Bragg equation are equivalent in that they both describe the relation between the lattice vectors and the scattering vector for an X-ray reflection to occur. For the sake of simplicity, we have considered the cubic lattice case, but it should be emphasized that the Bragg equation is valid for any lattice structure. Equation (2.5) can be also rewritten in terms of the momentum transfer parameter x, which is defined as

$$x = \frac{\sin(\theta/2)}{\lambda} \tag{2.6}$$

Inserting the equation (2.6) into equation (2.5), yields the following form for the Bragg equation

$$x = \frac{1}{2d_{hkl}} \tag{2.7}$$

Diffraction profiles are usually expressed as functions of the x parameter. In this way, there is a direct relation between peak positions and the interplanar distances. A peak at an x value can be observed for many couples (λ,θ) satisfying the (2.6). Therefore, X-ray diffraction may be measured in two ways: (a) angular dispersion, where the intensity of the scattered profile for monoenergetic X-rays is measured as a function of scattered angle and (b) energy dispersion, where the energy distribution of a polychromatic X-ray beam scattered through a fixed angle is measured. Using polychromatic X-rays sources permits reducing the measurement time since the number of photons emitted by these kind of sources is about four orders of magnitude larger than a laboratory monochromatic source [8].
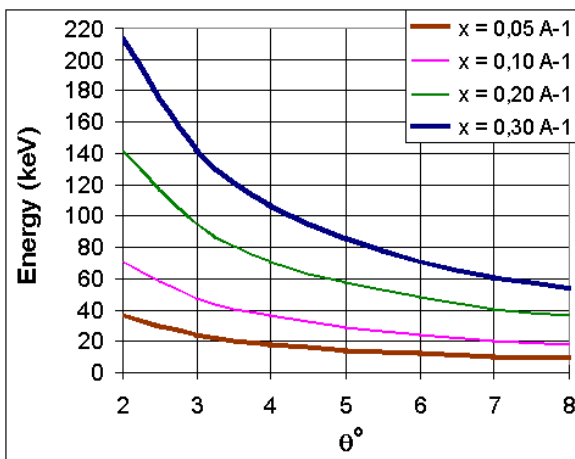
3. Diffraction angle and high voltage

Fig. 3.1. Evolution of energy values as functions of the diffraction angle θ for the x range comprised between 0.05 and 0.3 Å⁻¹.

The first parameters we have considered are the diffraction angle θ and the high voltage of X-ray source. In the energy-dispersive mode, once the working angle is fixed, the diffraction profile is measured as a function of the beam energy. Varying the angle θ implies, for a given material, translating the peak positions in the energy range. Now, from the literature [2,8] we know that diffraction effects are observed for x values in the range [0.05, 0.3 Å⁻¹] (some materials present isolated peaks up to 0.5 Å⁻¹ [8]). It is therefore interesting to look how the interval in x can be expressed as an interval in energy E for different angles θ. Using the equation (2.6) we can write

$$\Delta E(\Delta x,\theta) = 12.4 \times 1/(\sin(\theta/2))\Delta x \tag{3.1}$$

3

where Δx and ΔE are supposed to be expressed in units of Å^{-1} and keV, respectively. The graph of Fig. 3.1 shows the evolution of ΔE as a function of the angle θ. It emerges that increasing the angle will translate the peaks to lower energies. For example, if a given material presents a peak at 95 keV and for an angle of 3° (green line on Fig. 3.1), the same peak will be measured at 47 keV if the angle is moved to 6°. This property is clearly pointed out when looking at the available material spectra databases ([15,16] being some examples). In particular, the database furnishes the structure factor $\left|F(q_i)\right|^2$ values for all peaks q_i, i.e. for all interplanar distances d_i, characterizing a medium. As an example, on Fig. 3.2 the $\left|F(E_i)\right|^2$ values of the γ-RDX ($C_3H_6N_6O_6$) for different angles θ are reported. It should be pointed out that each graph of Fig. 3.2 reports the same ensemble of $\left|F_i\right|^2$ values; they only differ in the peak energy position. For example the peak at 100 keV and $\theta = 3°$, moves to 60 keV when $\theta = 5°$. We remark two important properties when decreasing the angle θ: i) the inter-peak distance increases; ii) the peak positions are translated to higher energies. Since the X-ray attenuation is stronger at low energies, it is preferable to work at a small diffraction angle. Now, reducing θ will require to increase the voltage of the X-ray source to exploit the high energy peaks. For a portable system the case $\theta \sim 3°$ seemed to be a good compromise between the desire of prevent the attenuation effects and the need not to exceed the tube voltage to values larger than 160 kV.
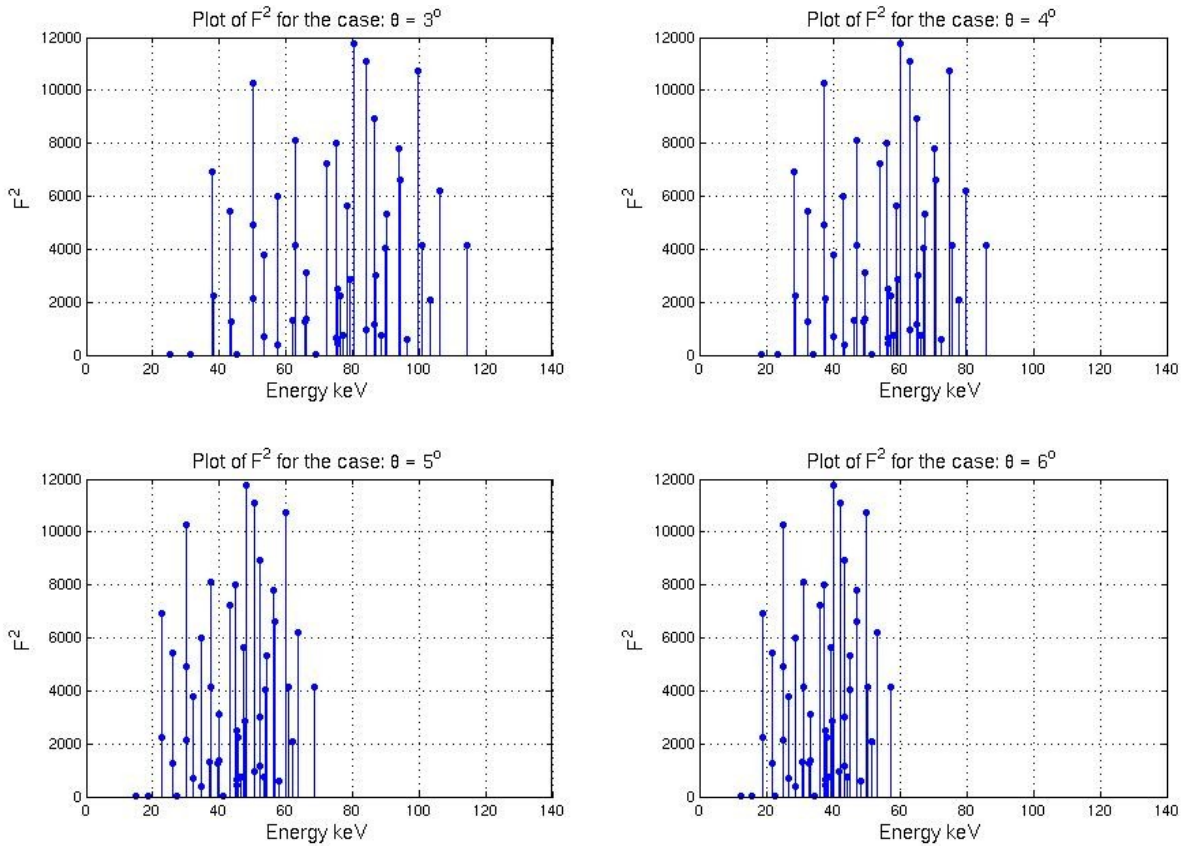

Fig.3.2. The structure factor values $\left|F_i\right|^2$ of γ–RDX as functions of the beam energy for different angles θ.

4. System momentum transfer resolution

In a diffraction-based inspection device, another important parameter is the resolution with which the spectra are collected. The diffraction patterns are characterized by a total uncertainty σ_x, which depends on the uncertainties in the photon energy E and in the scattering angle θ, by the usual

formula

$$\sigma_x = \sqrt{(\tfrac{\partial}{\partial E}x)^2(\sigma_E)^2 + (\tfrac{\partial}{\partial \theta}x)^2(\sigma_\theta)^2} \qquad (4.1)$$

Using the x definition (2.6), we can write in the small angle approximation

$$\sigma_x / x = \sqrt{(\sigma_E/E)^2 + (\sigma_\theta/\theta)^2} \qquad (4.2)$$

In the energy-dispersive mode the uncertainty in the energy measurement depends on the energy resolution ΔE of the detector. ΔE is defined as the *FWHM* of the detector energy response, which has typically a Gaussian shape. For a normal distribution, the *FWHM* is equal to 2.35 times the standard deviation σ. Multiplying the (4.2) by 2.35, we can write:

$$(\Delta x / x) = \sqrt{(\Delta E / E)^2 + (\Delta \theta / \theta)^2} \qquad (4.3)$$

The *FWHM* for the CZT detector remains limited to 2.7 keV by electronic noise from both detector and preamplifier [11]. The remaining parameter to be selected for the portable system is then the angular resolution $\Delta \theta$. In practice, the term $\Delta \theta$ is determined by two parameters: the collimation length (we will detail in the section 6 the relation between $\Delta \theta$ and the collimator requirements) and the size of the collimator slit. In principle, $\Delta \theta$ can be made arbitrarily small by arranging the collimation length sufficiently large [8]. However, for the portable system there was the desire of a collimation length as small as possible. In addition, reducing $\Delta \theta$ will reduce the mean number of detected photons (for the same acquisition time), increasing then the photon noise. Since the aim of recording the diffraction spectra is the material identification, we have studied the influence of the angular resolution on the "shape" of the diffraction patterns. For this purpose, the momentum resolution has been modeled as follows

$$(\Delta x / x) = (\Delta E / E)(1 + k) \qquad (4.4)$$

where k is a dimensionless parameter expressing the system resolution as a proportion of the detector energy resolution. The case $k = 0$ represents an ideal collimator giving an angle selection without uncertainty. In practice k is larger than zero. Using the equation (4.4) allows writing the following linear equation for the term Δx

$$\Delta x (\mathring{A}^{-1}) = \tfrac{1}{12.4} \sin(\theta/2) \Delta E (keV)(1 + k) \qquad (4.5)$$

For the sake of completeness, we would like to point out that Δx is not constant over the x range, though ΔE and $\Delta \theta$ being fixed. We have introduced the model of equation (4.4) in order to evaluate a "mean" Δx permitting to compute the convolution between ideal spectra and a Gaussian curve, whose *FWHM* is set equal to Δx. We name "ideal spectra" the set of $|F(x_i)|^2$ data. Computing Δx for different k values by equation (4.5) needs to set ΔE and θ. In the example of Fig. 4.1, ΔE has been set to 2.7 keV and θ to 3°. Fig. 4.1 shows the diffraction spectra of Tetryl ($C_7H_5N_5O_8$) obtained in the ideal and real conditions. We see that for large k values the characteristic material peaks start to melt together rendering the material identification more difficult.

It is not obvious to clearly establish the maximum k value beyond which the diffraction patterns are no longer exploitable. The possibility to perform material identification depends also on the noise content of acquired data and on the goodness of post-processing tools. However, after the analysis of a large set of materials, we have decided to retain the value of $k = 0.5$.
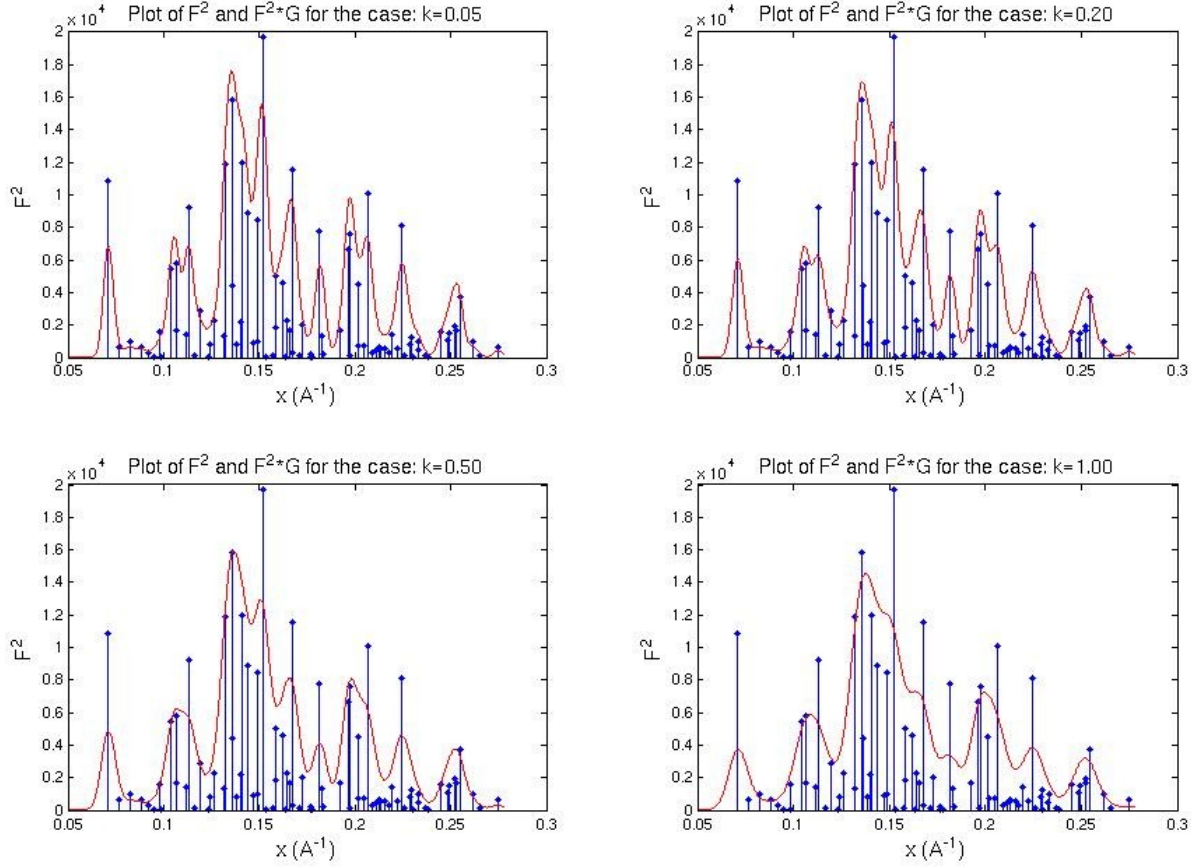
5

Fig.4.1. Tetryl diffraction spectra. The ideal spectra (blue line) are compared with the real (red line) ones for k ranging from 0.05 to 1. The corresponding values for Δx are : 0.0060, 0.0068, 0.0085 and 0.011 Å⁻¹ for k = 0.05, 0.20, 0.50 and 1.00, respectively.

Combining the equations (4.3) and (4.4), we obtain for $\Delta\theta$:

$$\Delta\theta = \theta\sqrt{k(k+2)}(\Delta E/E) \tag{4.6}$$

Computing $\Delta\theta$ for $k = 0.5$ and for experimental conditions of Fig. 4.1 gives $\Delta\theta = 0.1°$.

It is interesting to look also how Δx varies as a function of the diffraction angle. Expressing E in terms of x and θ, the (4.3) can be rewritten as

$$\Delta x = \sqrt{c^2\theta^2(\Delta E)^2 + x^2(\Delta\theta/\theta)^2} \tag{4.7}$$

where $c = 1/(2\times12.4)$ and Δx and ΔE are supposed to be expressed in units of Å⁻¹ and keV, respectively. On Fig. 4.2 the $\Delta x(\theta)$ curves for the two extreme x value of 0.05 and 0.3 Å⁻¹ and for two different ΔE (those of detectors based on CZT and Ge) are reported. The Fig. 4.2 two graphs are plotted for $\Delta\theta = 0.03°$(a) and 0.15°(b).

From Fig. 4.2, we can see that when θ increases, Δx is mainly due to the first term in the square root of equation (4.7) with a consequent lost in the x dependence while at small angle, Δx is mainly due to the second term in the square root of equation (4.7) and we loose here the ΔE dependence. On Fig. 4.2 we can see that each curve presents a minimum value, which is a function of $\Delta\theta$, ΔE and x according to

$$\theta_{min} = \sqrt{\frac{x}{c}\frac{\Delta\theta}{\Delta E}} \qquad (4.8)$$

An interesting property emerging from these curves is the fact that assuming the $\Delta\theta$ to be fixed by the collimation system, there is an optimal working angle minimizing Δx. For example, from the system resolution point of view, working with the CZT detector gives an optimal angle of 5° for a collimator angular resolution set to 0.15°.

Hence, it emerges that the choice of the diffraction angle has to take into account an additional aspect: reducing θ will need an efficient collimation system, otherwise the momentum resolution will be too worse for the material identification.

Our choice of $\theta = 3°$, has been driven from beam attenuation considerations (see section 3). For this angle we found that $\Delta\theta$ has to be set to 0.1° if we want a mean Δx of 0.0085 Å^{-1}, which should result in diffraction profiles like those of Fig. 4.1(k = 0.50). If we insert these values in the equation (4.7) (with $\Delta E = 2.7$ keV), we obtain Δx comprised between 0.0059 and 0.0115 Å^{-1} for x ranging from 0.05 to 0.3 Å^{-1}. In particular, $\Delta x = 0.0076$ Å^{-1} for the intermediate x value of 0.15 Å^{-1}.
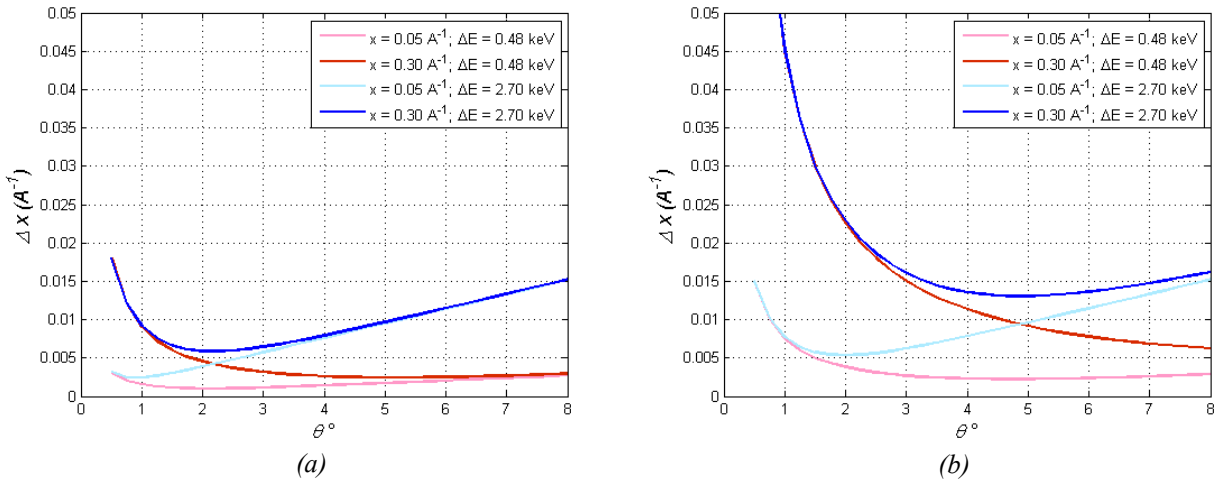

(a)   *(b)*

Fig. 4.2. $\Delta x(\theta)$ curves for the two extreme x values of 0.05 and 0.3 Å^{-1}, for two different ΔE (CZT and Ge based-detectors). Two different angular resolutions are tested: $\Delta\theta = 0.03°$(a) and $\Delta\theta = 0.15°$(b).

5. Experimental configuration

On Fig. 5.1 a schematic representation (not to scale) of the system configuration is reported. A source collimator defines a pencil beam with an angular aperture Γ. The scattered radiation is measured at an angle θ by means of the detector collimator, which is characterized by an angular acceptance α. The energy distribution of the scattered X-rays is measured by the CZT detector. The source collimator consists of a block of an attenuating medium (tungsten) with a central hole a_e in diameter. We name L_e the source collimator length. The resulted angular opening Γ is defined by the following equation:

$$\tan(\Gamma/2) = \frac{a_e}{L_e} \qquad (5.1)$$

This equation is true, if the source lateral dimension D is larger than the parameter d (see Fig.5.1), where $d = b \times \tan(\Gamma/2)$ and b is the source-collimator distance. The condition $D > d$ is largely satisfied for our case.
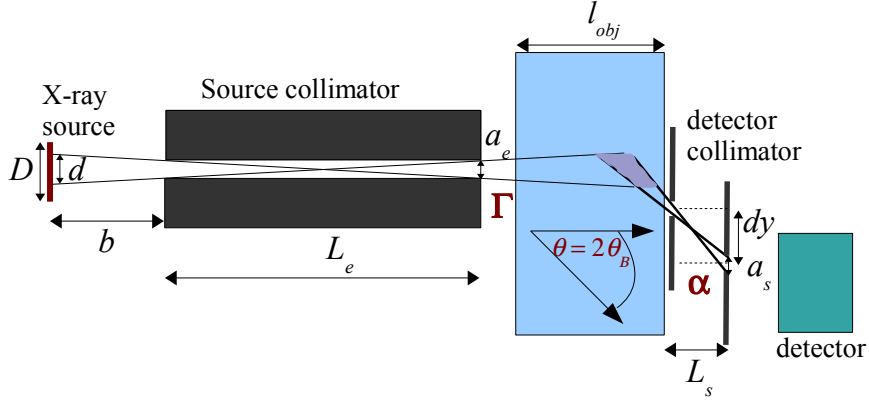
Fig. 5.1. Schematic representation (not to scale) of the system configuration.

The collimator in front of the detector is modeled as a system composed by two attenuating plates with a circular aperture a_s in diameter. The distance L_s between the plates, the relative offset dy between the two plates apertures, and the diameter a_s define the scattered angle θ and the collimator angular opening α by the following equations

$$\tan(2\theta) = \frac{2L_s\,dy}{L_s^2 - dy^2 + a_s^2}$$
(5.2)

$$\tan(\alpha) = \frac{2L_s\,a_s}{L_s^2 + dy^2 - a_s^2}$$
(5.3)

In the next section, the relation between the desired angular resolution and the collimators parameters will be discussed.

6. Angular resolution and collimators requirements

In section 4, the angular resolution $\Delta\theta$ has been defined as 2.35 times the uncertainty σ_θ on the angle selection. Since our system contains two collimators acting independently, we can write for the total angular resolution

$$\Delta\theta = \sqrt{(\Gamma/2)^2 + (\alpha/2)^2}$$
(6.1)

In analogy to the previous formalism, we decided to model $\Delta\theta$ by means of a dimensionless parameter k'

$$\Delta\theta = \alpha/2\,(1 + k')$$
(6.2)

where k' represents the angular resolution percentage caused by the source collimator relatively to the detector collimator. The special case $k' = 0.414$ corresponds to identical angular openings for the two collimators: $\Gamma = \alpha$.

On Fig. 6.1(a) the Γ and α values as functions of k' and for two k values (0.05 and 0.5) are reported. The case $k = 0.05$ represents experimental conditions where the system resolution is mostly affected by the detector resolution (see section 4). The Fig. 6.1 curves were computed for a diffraction angle θ of 3° and a mean relative energy resolution $\Delta E/E$ of 3%. Once the collimators angular openings

8

are defined, there are large sets of possible values for the collimation lengths L_e and L_s and the diameters a_e and a_s satisfying the equations (5.1), (5.2) and (5.3).

However, for the purpose of our project there is the necessity of a collimation length as small as possible. For this reason, we focused our attention on the case $a_e = a_s = 100$ microns, which represents the manufacturing limit for circular apertures in tungsten plates. Fig. 6.1(b) shows the plots for the collimation length L_e and L_s as functions of k' and for two k values: 0.05 and 0.5. As obviously expected, increasing k requires smaller L values. The case $k = 0.05$ implies collimation length values too large for our system requirements. It is interesting to point out that the case $k' = 0.414$ yields a minimum for the "total" collimation length $L_{tot} = L_e + L_s$.

7. Discussion

A multi-parametric optimization study for the experimental configuration of a portable inspection device has been presented. The study concerns the EDXRD modality, which gives a specific signature of the material. The aim was to select the best suited experimental conditions for the system purposes. In order to clearly identify the role of each parameter on the expected measurements, the model based on the kinematic theory of diffraction has been considered.
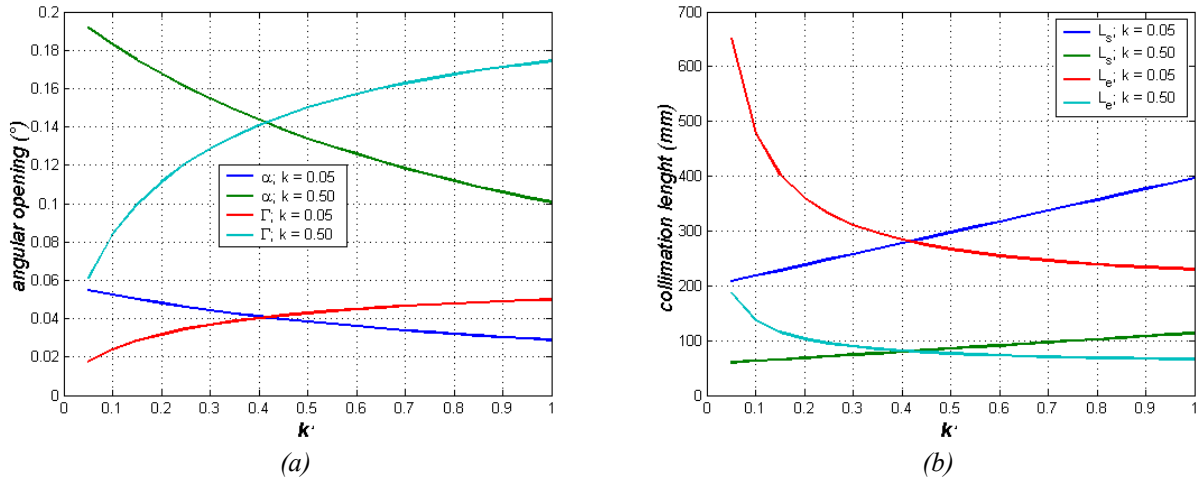

Fig. 6.1. Angular openings α and Γ (a) and collimation lengths L_e and L_s (b) as functions of the parameter k' for different k values.

The first parameters we investigated were the diffraction angle θ and the X-ray tube high-voltage. It has been pointed out that the diffraction angle defines the energy range the peaks will be found in. Increasing θ will translate the peaks to lower energies where the beam attenuation effects are more severe. As soon as the suitcase will contain an attenuating medium into the X-ray trajectory, the intensity of the low energy peaks will be drastically reduced (for example there is a difference of eleven orders of magnitude between the X-ray attenuation through 1 cm of Fe at 40 and 80 keV. Now at a working angle of 6° the diffraction peaks are suited at energies smaller than 60 keV; while at 3° there are about the half of peaks at energies larger than 80 keV). Therefore, a small working angle (~ 3°) and a high voltage ≥ 160 kV are recommended.

As it pertains to the angular resolution, our approach was to identify an angular resolution limit beyond which the diffraction patterns are no longer exploitable, and then to compute the collimators parameters for the considered $\Delta\theta$. After the analysis of a large number of spectra, we selected for the angular resolution the value of 0.1°.

Collimators are essentially characterized by two quantities, the diameter of the aperture into the

attenuating medium composing the collimator and the collimation length, i.e. the collimator dimension along the X-ray trajectory. Thus, for a fixed angular aperture, reducing the diameter will reduce the distance L. We focused our attention on the case $a_e = a_s = 100$ microns, which represents the manufacturing limit for circular apertures in tungsten plates. As shown on Fig.6.1(b), the case $k' = 0.414$ yields a minimum for the "total" collimation length. Therefore, we decided to share out equally the angular resolution between the source and the detector collimators. In this case we obtain for both the collimation lengths L_e and L_s the value of 8 cm. As future work, we envisage to investigate the limit for the angular resolution and its relation with the data noise content and the post-processing tools developed for the material discrimination.

Acknowledgements

References

1) R D Luggar, J A Horrocks, R D Speller, and R J Lacey, 'Low angle X-ray scatter for Explosives Detection: a Geometry Optimization', Appl. Radiat. Isot. 48, pp. 215-224 (1997)
2) C H Malden and R D Speller, 'A CdZnTe array for the detection of explosives in baggage by energy-dispersive X-ray diffraction signatures at multiple scatter angles' Nucl. Instrum. Methods Phys. Res. A 449, pp. 408-415 (2000)
3) I D Jupp, P T Durrant, D Ramsden, T Carter, G Dermody, I B Pleasants, and D Burrows, 'The non-invasive inspection of baggage using coherent X-ray scattering', IEEE Trans. Nucl. Sci. 47, pp. 1987-1994 (2000)
4) E Cook, R Fong, J Horrocks, D Wilkinson, and R Speller, 'Energy-dispersive X-ray diffraction as a mean to identify illicit materials: A preliminary optimisation study', Appl. Radiat. Isot. 65, pp. 959-967 (2007)
5) A Jenkins, and P W Stephens, 'X-ray diffraction inspection system', U. S. Pat. No. 5,007,072 (1991)
6) G Harding, 'Device for measuring the pulse transfer spectrum of elastically scattered X-ray quanta' U. S. Pat. No. 5,394,453 (1995)
7) A A Husseiny, E D Stevens, and Z A Sabri, 'Detection of concealed explosives and contraband', U. S. Pat. No. 5,692,029 (1997)
8) G Harding and B Schreiber, 'Coherent X-ray scatter imaging and its applications in biomedical science and industry', Radiat. Phys. Chem. 56, pp. 229-245 (1999)
9) G Harding, 'X-ray scatter tomography for explosives detection', Radiat. Phys. Chem. 71, pp. 869-881 (2004)
10) G Harding, 'X-ray diffraction imaging – a multi-generational perspective', Appl. Radiat. Isot. 67, pp. 287-295 (2009)
11) G Montémont, C Moulin, J Isard, and L Verger, 'A Digital Pulse Processing System Dedicated to CdZnTe Detectors', IEEE Trans. Nucl. Sci. 52, pp. 2017-2022 (2005)
12) B D Cullity, 'Elements of X-ray diffraction', (Addison-Wesley, Reading, 1956) pp. 123-136
13) B E Warren, X-Ray Diffraction, Addison-Wesley, Reading, MA, 1969
14) M Birkholz, Thin Film Analysis by X-Ray Scattering, Copyright © 2006 WILEY-VCH Verlag GmbH & Co. KGaA, Weinheim ISBN: 3-527-31052-5
15) http://www.crystallography.net
16) http://www.escher.epfl.ch/eCrystallography